RSC Advances

PAPER

View Article Online
View Journal | View Issue

Cite this: *RSC Adv.*, 2017, **7**, 53126

Tin-based materials supported on nitrogen-doped reduced graphene oxide towards their application in lithium-ion batteries†

Xiaoxia Zuo,[a] Bao Li,[a] Kun Chang,*[b] Hongwei Tang[a] and Zhaorong Chang *[a]

Received 28th September 2017
Accepted 2nd November 2017

DOI: 10.1039/c7ra10731e

rsc.li/rsc-advances

Recently, nitrogen-doped graphene has attracted significant attention for application as an anode in lithium-ion batteries due to effective modulation of the electronic properties of graphene. Herein, we report a facile route to successfully synthesize a series of tin-based materials (including Sn, SnO_2, and SnS_2) supported on N-doped reduced graphene oxide (N-rGO). Field emission scanning electron microscopy (FESEM) and transmission electron microscopy (TEM) images indicated that the Sn-based materials were uniformly and tightly dispersed on the surface of N-rGO. When used as an anode in LIBs, the electrochemical performances of the proposed electrodes were systematically investigated and compared. The results show that among these electrodes, SnS_2/N-rGO with a matched layered structure delivers the best performance with not only high specific capability but also excellent cycling stability.

1. Introduction

Rechargeable lithium-ion batteries (LIBs) are a promising power technology for future applications. They have also attracted extensive attention as power sources for high-power tools and electric vehicles. Graphitic materials are extensively used as commercial anode materials for LIBs due to their flat and low potential profile as compared to that of lithium and structural stability during cycling. However, the small theoretical specific capacity of graphite (372 mA h g^{-1}) necessitates the search of alternative negative electrodes.[1] During the past few decades, numerous research efforts have been carried out towards exploring novel anode materials, such as amorphous carbon, metal oxides, metal sulfides, and metals or alloys, with high specific capacity;[2–8] moreover, ideal electrodes that possess not only high capacity but also lower potential profile have been prepared using tin (Sn)-based and silicon (Si)-based materials, as shown in Fig. S1 (ESI).† However, the large volume changes of both metals during the lithiation process restrict the improvement in cycling stability, especially for Si-based electrodes in which the volume change can reach up to 420%, severely destroying the structure of the electrodes.[9–13]

Sn-based materials have attracted growing research interest for use in LIB anodes due to their multi-type compounds such as SnO_2 and SnS_2, which can buffer the large volume change to some extent.[14–17] Moreover, the discovery of reduced graphene oxide (rGO) in recent years has led to the development of a significant number of graphene-based metal, metal oxides, or metal sulfides for use as LIB anodes due to the unique physical and chemical properties and potential of rGO for applications in electronic devices and sensors. The results have generally been promising towards the improvement of their specific capacity and cycling stability.[8,18–20] To further enhance the properties of rGO, element (such as sulfur, boron, and nitrogen) doping *via* chemical substitution has been used beyond just morphology and size control, and nitrogen doping is shown to be particularly effective in modulating the electronic properties of graphene.[21] Based on previous reports on Sn-based materials supported on rGO or nitrogen-doped rGO (N-rGO), the most frequently used preparation method is to use rGO as a template and subsequently subject it to a reduction reaction to form Sn-based rGO composites.[22–30] Although Sn-based materials prepared using this method can be uniformly dispersed on the surface of rGO, the number of remaining oxygen functional groups on rGO will restrict the electronic conductivity and electrochemical performance for the LIB anodes.[21]

Therefore, our current study was aimed at using the as-prepared rGO and N-rGO obtained *via* a thermal exfoliation method as the templates to synthesize Sn-based materials supported on rGO or N-rGO. However, this attempt was unsuccessful while preparing SnO_2/rGO, where the SnO_2 nanoparticles could not be directly anchored on the surface of rGO. This may be attributed to the smooth surface of rGO obtained *via* the thermal exfoliation method. Herein, a series of Sn-based materials (including Sn, SnO_2, and SnS_2) supported on N-rGO were successfully synthesized. Field emission scanning

[a]*Collaborative Innovation Center of Henan Province for Green Manufacturing of Fine Chemicals, School of Chemistry and Chemical Engineering, Henan Normal University, Xinxiang 453007, P. R. China. E-mail: czr_56@163.com*

[b]*National Institute for Materials Science (NIMS), 1-1 Namiki, Tsukuba, Ibaraki, 305-0044, Japan. E-mail: chang.kun@nims.go.jp*

† Electronic supplementary information (ESI) available. See DOI: 10.1039/c7ra10731e

electron microscopy (FESEM) and transmission electron microscopy (TEM) images indicated that the Sn-based materials were uniformly and tightly dispersed on the surface of N-rGO. When used as LIB anodes, the electrochemical performance of the proposed electrodes was systematically investigated and compared. The results show that among these electrodes, SnS_2/N-rGO with a matched layered structure delivered the best performance, with not only high specific capability but also excellent cycling stability.

2. Experimental

2.1 Synthesis of rGO and N-rGO

RGO and N-rGO were prepared following literature procedures.[21] Briefly, graphite oxide powder was first synthesized using the modified Hummers method.[31] Then, the graphite oxide powder was heated at 1050 °C for 30 s under an Ar atmosphere to obtain rGO. N-rGO was further obtained by heating rGO under high purity ammonia mixed with Ar at 900 °C for 4 h.

2.2 Synthesis of the Sn-based N-rGO composites

To synthesize the SnO_2/N-rGO composite, 0.38 g of $SnCl_2$ and 2 mL of 0.5 M HCl were dissolved in 80 mL of deionized water, and then, the abovementioned N-rGO powder was added to the mixture. After ultrasonication and stirring for 30 min, the mixture was transferred to a 100 mL Teflon-lined stainless steel autoclave, sealed tightly, and heated at 180 °C for 12 h. After cooling down to room temperature naturally, the black precipitate was obtained by centrifugation, washed with deionized water and ethanol, and then dried in a vacuum oven at 80 °C for 24 h. Finally, the products were annealed at 300 °C for 1 h under an Ar atmosphere. In the control experiment, the Sn/N-rGO composite was also prepared using the same abovementioned procedure with N_2H_4 and H_2 protection in the synthetic route, and the SnS_2/N-rGO composite was prepared using the same procedure with L-cysteine as the S source.

2.3 Characterization

Samples were characterized *via* X-ray diffraction (XRD; Rigaku RU-200BVH diffractometer employing a Cu-K_α source), field emission scanning electron microscopy (FESEM, Hitachi S-4800), transmission electron microscopy (TEM, TECNAI G2 F30, Japan), energy dispersive X-ray spectroscopy (EDX, GENESIS 4000), Raman spectroscopy (Horiba-Jovin Yvon T64000) and X-ray photoelectron spectroscopy (XPS, ULVAC-PHI, Japan).

2.4 Electrochemical measurements

The negative electrodes for the battery tests were composed of Sn-based materials, acetylene black, and polyvinylidene fluoride (PVDF) in a weight ratio of 75 : 10 : 15. The mixture of the active material, acetylene black, and PVDF was ground for 2 h in an agate mortar. The mixture was then dried in a vacuum oven at 80 °C for 4 h to remove any moisture. After this, NMP was added

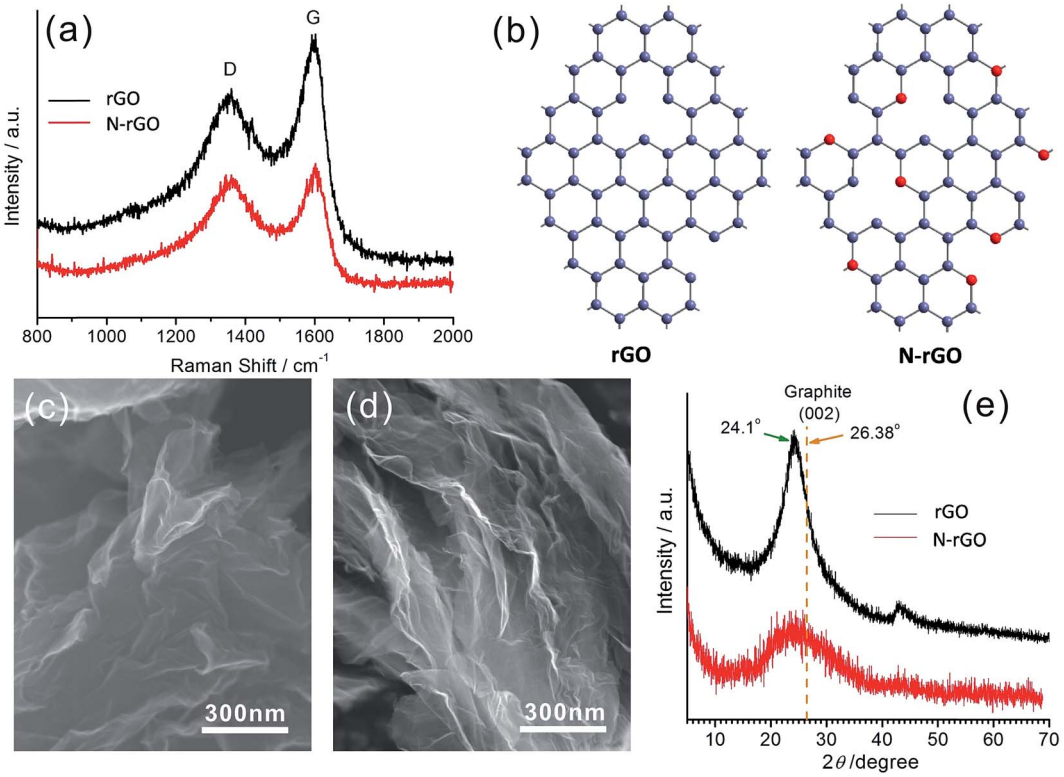

Fig. 1 (a) The Raman spectra of rGO and N-rGO. (b) A schematic of the molecular structures of rGO and N-rGO. SEM images of (c) rGO and (d) N-rGO. (e) XRD patterns of rGO and N-rGO.

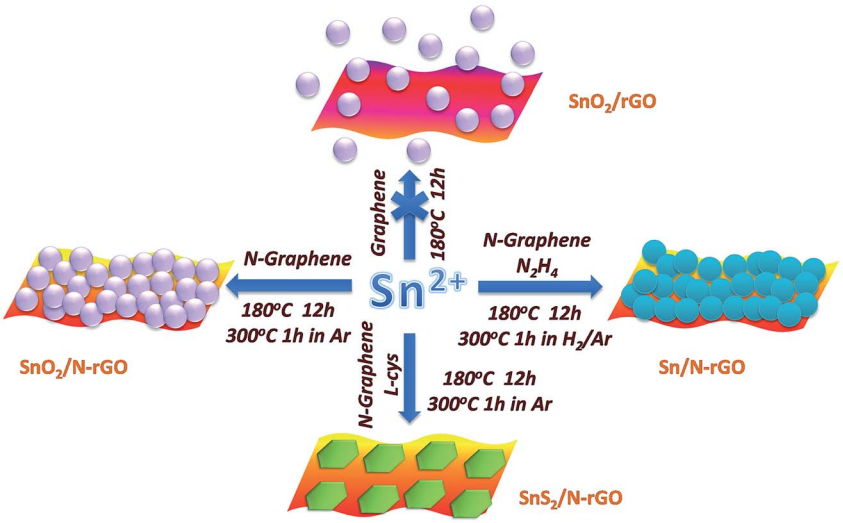

Fig. 2 A schematic of the synthetic routes used to prepare the Sn-based materials supported on rGO and N-rGO.

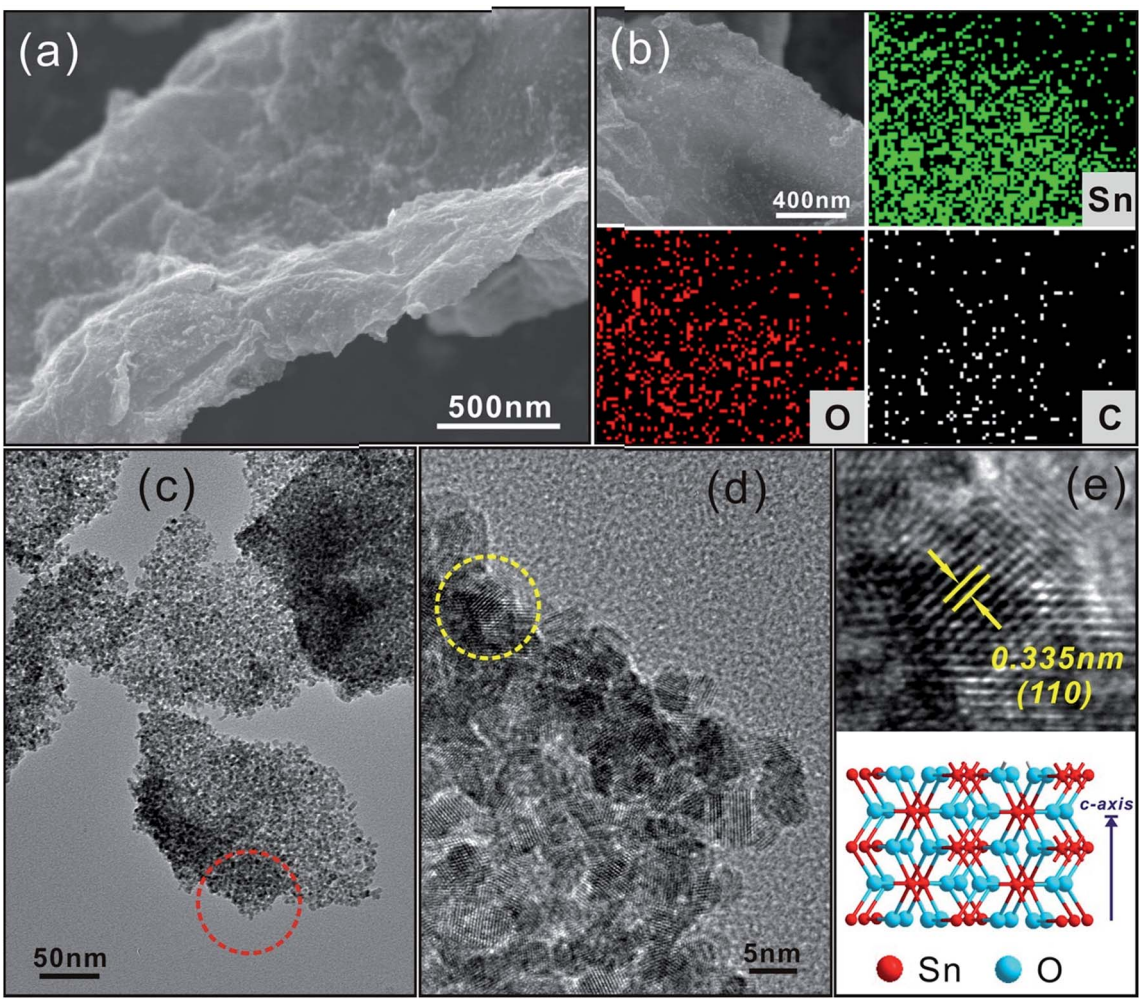

Fig. 3 The morphology and structure of SnO_2/N-rGO: (a) SEM image of SnO_2/N-rGO, (b) EDS mapping for each element, (c) TEM image of the SnO_2/N-rGO composite, (d) the magnified area shown in (c), (e) the HRTEM image of the selected area shown in (d), and a schematic of the molecular structure of SnO_2.

to form a slurry, which was subsequently spread onto a copper foil with a thickness of 0.1 mm and a diameter of 12 mm, dried at 80 °C in a drying oven for 2 h, compacted using a hydraulic press, and then dried again at 120 °C for 12 h in a vacuum drying chamber. Button cells (2025R) containing a Li foil as a counter electrode, polypropylene film (Celgard 2400) as a separator, and 1 M (mol L^{-1}) $LiPF_6$ in a mixture of ethylene carbonate/dimethyl carbonate/diethyl carbonate (EC/DMC/DEC 1 : 1 : 1 by volume) as an electrolyte were assembled in an argon-filled glovebox. Constant-current charge and discharge tests were performed using a cell test system (Land CT2001A) in the potential range between 0.005 and 3.0 V. Cyclic voltammetry (CV) tests were carried out using an electrochemical workstation (CHI 660C) over a potential range from 0.005 to 3.0 V at a scan rate of 0.1 mV s^{-1}. Electrochemical impedance tests were also performed using an electrochemical workstation (CHI 660C) over the frequency range from 0.01 Hz to 100 kHz at an amplitude of 5 mV.

3. Results and discussion

The proposed rGO and N-rGO were synthesized using the method described in the Experimental section. According to the calculation in XPS spectrum of N-rGO, the atomic ratio of the doped nitrogen was estimated to be 2.3 at% (Fig. S2†). Fig. 1 shows the characterization results for the as-prepared rGO and N-rGO. Upon comparing their Raman spectra shown in Fig. 1a, it was found that the D band observed at approximately 1350 cm^{-1} was disorder-induced and attributed to the structural defect sites on the rGO plane. The G band observed at approximately 1600 cm^{-1} is commonly observed for all graphitic structures and attributed to the E_{2g} vibrational mode present in the sp^2-bonded graphitic carbons. The intensity ratio of the D peak to G peak, *i.e.* I_D/I_G, provides an indication of the amount of structural defect sites and is a quantitative measure of edge plane exposure. It can be clearly observed from Fig. 1a that the I_D/I_G ratio of N-rGO is obviously larger than that of rGO as a result of the structural defect sites caused by the incorporation of heterogeneous nitrogen atoms into the rGO layers. Their corresponding molecular structures are schematically illustrated in Fig. 1b, where the red balls represent the nitrogen atoms. At high temperatures, the partial active carbon atoms in rGO are easily replaced by the nitrogen atoms in ammonia gas to form N-rGO with more defects and vacancies. Upon comparing the FESEM images of rGO (Fig. 1c) and N-rGO (Fig. 1d), it has also been found that N-rGO possesses a rougher and more wrinkled surface than rGO. Moreover, after nitrogen doping, the rGO nanosheets become thinner, which can be observed from the XRD patterns shown in Fig. 1e. The diffraction peaks observed at $2\theta = 24.1°$, which are attributed to the (002) plane of the rGO and N-rGO nanosheets, have the slightly larger interlayer distance than that of graphite, with the diffraction peak of (002) at $2\theta = 26.38°$. In addition, the (002) peak intensity of N-rGO was obviously lower than that of rGO;

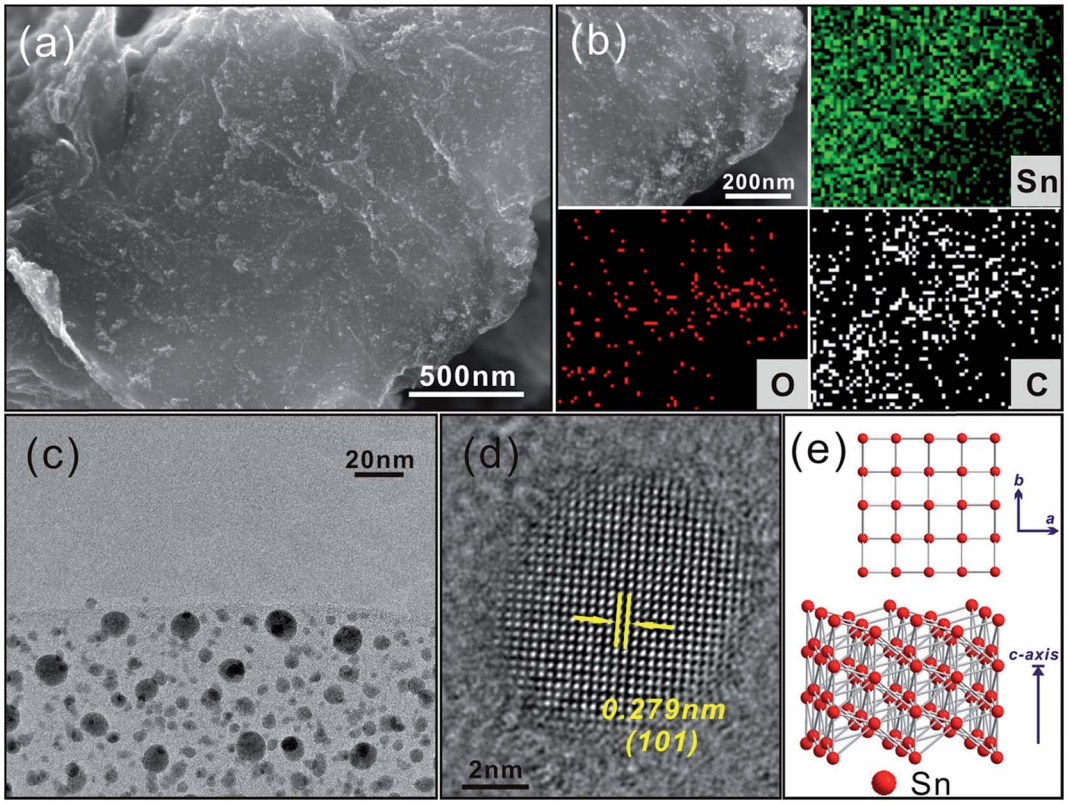

Fig. 4 The morphology and structure of Sn/N-rGO: (a) SEM image of Sn/N-rGO, (b) corresponding EDS mapping for each element, (c) TEM image of the Sn/N-rGO composite, (d) HRTEM image of Sn/N-rGO, and (e) a schematic of the atomic structure of Sn.

this indicated that the restacking degree of the N-rGO nanosheets along *c*-axis was lower than that found in the case of the rGO nanosheets as well as illustrated that the nanosheets for N-rGO were more thinner.

Using N-rGO as a template, the Sn-based materials were anchored *in situ* on the surface of N-rGO *via* a solution-phase method. Fig. 2 illustrates schematically the synthesis routes used to prepare the Sn-based materials supported on N-rGO, in which Sn^{2+} ions are the starting materials. While using rGO as the template, the hydrolyzed SnO_2 nanoparticles were not adsorbed on the surface of the rGO nanosheets. It can also be observed in Fig. S3† that the SnO_2 nanoparticles are separated from the rGO nanosheets. As abovementioned, this may be attributed to the smooth surface of the rGO nanosheets obtained through the thermal exfoliation process, which does not provide nucleation sites for the SnO_2 nanoparticles. Thus, N-rGO with more defect sites and vacancies was used as the template for the nucleation of SnO_2 nanoparticles.[32]

Fig. 3 shows the morphology and structure of SnO_2/N-rGO. The FESEM image, as shown in Fig. 3a, indicates that the SnO_2 nanocrystals are densely anchored on the surface of the N-rGO nanosheets; this is caused by the large number of defects and vacancies in N-rGO. The elemental mapping images shown in Fig. 3b reveal that the Sn, O, and C elements are uniformly dispersed on the N-rGO nanosheets. The TEM images, as shown in Fig. 3c and d, show that the average size of the SnO_2 nanocrystals is around 3–4 nm, and from the HRTEM image (Fig. 3e), it can be seen that the lattice fringes of 0.335 nm correspond to the (110) planes of tetragonal SnO_2. The XRD pattern of SnO_2/N-rGO is shown in Fig. S4.† All the peaks can be indexed to tetragonal SnO_2 (JCPDS 41-1445), and the corresponding molecular structure is illustrated in Fig. 3e.

The Sn/N-rGO composite was obtained from SnO_2/N-rGO by annealing at 300 °C in H_2/N_2 for 1 h. The SnO_2 nanoparticles were reduced to Sn metal under H_2 during the high temperature treatment. Fig. 4 shows the morphology and structure of Sn/N-rGO, where it can be seen in Fig. 4a that the reduced Sn metal nanoparticles are homogeneously distributed on the surface of N-rGO. The element mapping images shown in Fig. 4b reveal that the composites mainly contain the elements Sn and C as well as a small amount of O derived from the oxygen functional groups of N-rGO and non-reduced SnO_2. The TEM image in Fig. 4c indicates that the Sn particle size ranges from 5 to 10 nm, and from the HRTEM image (Fig. 4d), it can be seen that the lattice fringes of 0.279 nm correspond to the (101) planes of tetragonal Sn. Fig. S5† shows the XRD pattern of the Sn/N-rGO

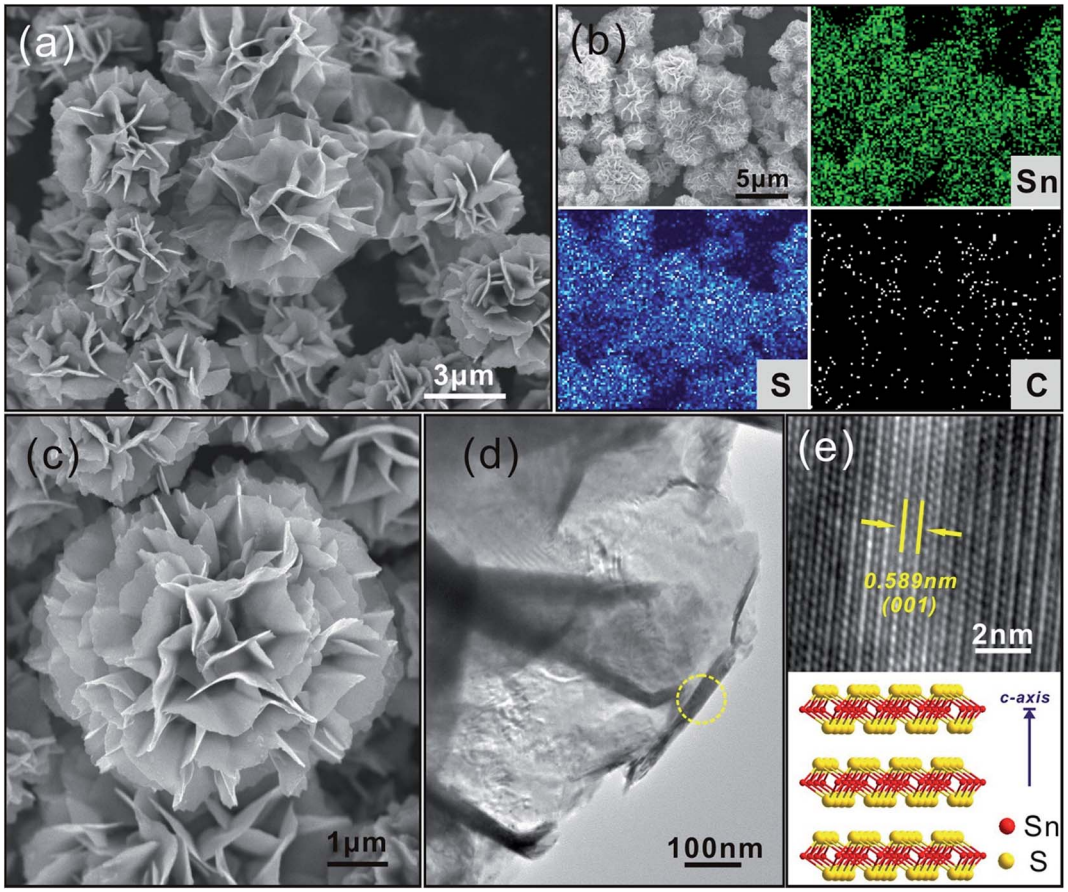

Fig. 5 The morphology and structure of SnS_2/N-rGO: (a) SEM image of SnS_2/N-rGO, (b) EDS mapping for each element, (c) the enlarged SEM image of the flower-like SnS_2/N-rGO composite, (d) TEM image of the SnS_2/N-rGO sheets and (e) the HRTEM image of the selected area shown in (d), and a schematic of the molecular structure of SnS_2.

composite, where it can be observed that all the diffraction peaks for the composites correspond well to the tetragonal crystalline phase of Sn (JCPDS 04-0673), which corresponds to the molecular structure illustrated in Fig. 4e.

Using a similar process as that used to prepare SnO_2/N-rGO, SnS_2/N-rGO was synthesized by adding L-cysteine (L-cys) as the sulfur source. Upon comparing the morphologies of SnO_2/N-rGO and Sn/N-rGO, which show zero-dimensional (0D) materials composited with two-dimensional (2D) materials, it has been observed that SnS_2/N-rGO shows a double 2D material composite structure. Fig. 5a provides a general view of the SnS_2/N-rGO composite, where it can be seen that the composite shows a three-dimensional (3D) architecture consisted of the curved nanosheets. According to previous reports,[3,33] the self-assembly of the 3D architecture materials was facile under the L-cys-assisted hydrothermal conditions due to the network structure of the L-cys molecule.

In this study, the self-assembly was promoted under the condition that layered SnS_2 and rGO were involved depending on their interactions. The elemental mapping images shown in Fig. 5b reveal that SnS_2/N-rGO mainly contains the elements Sn, S, and C, which are uniformly distributed in the composites. Fig. 5c and d indicate that SnS_2 and N-rGO deliver matched 2D layered structures, which are tightly composited together. The XRD pattern of SnS_2/N-rGO in Fig. S6† also shows that all the diffraction peaks can be attributed to layered hexagonal SnS_2 corresponding to the JCPDS card no. 23-0677. It can be calculated from the d spacing of the (001) peak at $2\theta = 15.1°$ according to the diffraction angles using the Bragg equation that the interlayer distance of SnS_2 is 0.59 nm, which is in accordance with the measurement results shown in the HRTEM image shown in Fig. 5e. When used as the anode material in an LIB, this 2D layered structure (Fig. 5e, illustration of the SnS_2 molecular structure) could buffer the volume change and improve the cycling stability of the electrodes.[34,35]

To investigate the effect of N-rGO on the electrochemical performance of the composites, we undertook electrical tests using different samples. According to the elemental analysis of EDS (Table S1†), it can be seen that the amount of N-rGO was lower than 3 wt% in the three composites; therefore, the Sn-based materials still acted as the major active electrode material in our experiments. Fig. 6 shows the first three charge/discharge profiles of the three composite samples between 0.01 and 3.0 V *vs.* Li^+/Li and their cycling behaviors at a current density of 100 mA h g^{-1}. All the specific capacities given below are calculated based on the whole composites. Upon comparing the three initial discharge curves of Sn/N-rGO, SnO_2/N-rGO, and SnS_2/N-rGO, it was found that an inconspicuous potential plateau appeared at 1.8 V for SnS_2/N-rGO (Fig. 6c), which could be attributed to the formation of Li_xSnS_2 when lithium ions were intercalated into the SnS_2 layers to some extent without causing phase decomposition.[36] For SnO_2/N-rGO (Fig. 6b), this

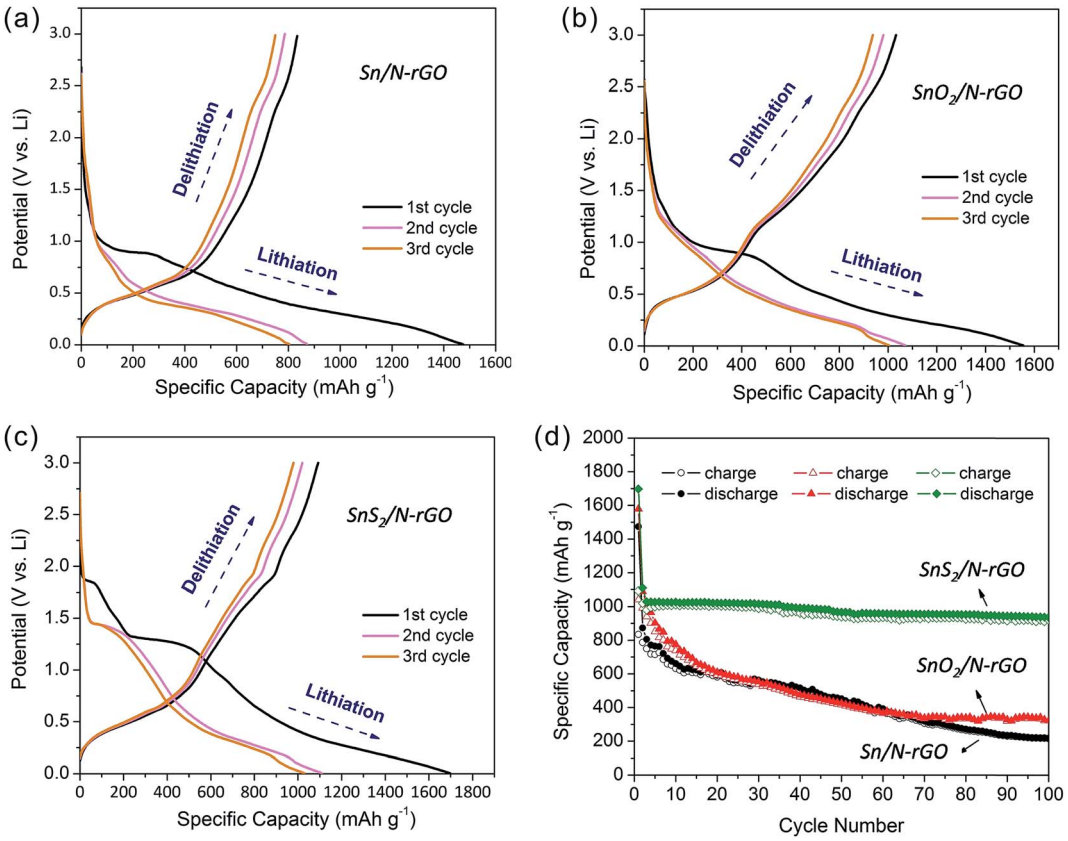

Fig. 6 The galvanostatic charge and discharge curves obtained for the (a) Sn/N-rGO, (b) SnO_2/N-rGO, and (c) SnS_2/N-rGO nanocomposites, and (d) their cycling behaviors at a current density of 100 mA h g^{-1}.

inconspicuous potential plateau appeared at 1.4 V, whereas no potential plateau was observed for Sn/N-rGO. The irreversible plateaus that emerged at 1.3 V for SnS_2/N-rGO and 1.0 V for SnO_2/N-rGO and Sn/N-rGO can be assigned to the formation of Sn and Li_2S or Li_2O,[37–39] where oxygen in the Sn/N-rGO composite originates from the oxygen functional groups in N-rGO (Fig. 4b). In the potential range from 0.01 to 0.5 V, lithium ions alloyed with the Sn metal form a series of Li–Sn alloys. During the subsequent cycles, the lithiation and delithiation process can be attributed to the following two reactions: Li_2S (or Li_2O) ↔ 2Li + S and Li_xSn ↔ xLi + Sn.[40] Correspondingly, the charge and discharge voltage plateaus characteristic for the three Sn-based N-rGO composites were assigned to their cyclic voltammograms curves (Fig. S7†).

In Fig. 6a–c, the initial charge capacity observed for Sn/N-rGO, SnO_2/N-rGO, and SnS_2/N-rGO was 834.3, 1041.3, and 1093 mA h g^{-1}, and the discharge capacity was 1473.8, 1579.2, and 1697.3 mA h g^{-1}, respectively. The initial irreversible capacity can be attributed to the formation of a solid electrolyte interface (SEI) layer and the side reactions of the electrolyte.[41] All three composites exhibit a high charge/discharge capacity when compared with bare Sn-based materials.[16,42–44] Among these, the SnS_2/N-rGO composite shows the highest specific capacity, and the higher capacity of SnO_2/N-rGO and SnS_2/N-rGO than Sn/N-rGO is assigned to the contribution of the O and S elements in the composites. The drastic enhancement in the specific capacity is attributed to the cooperation of N-rGO, which provides a large surface for anchoring the Sn-based materials uniformly and high conductivity for electron transport.[44,45] As is known, the main drawback of Sn-based materials as LIB electrodes is their volume change during cycling that leads to rapid capacity fading. Carbon materials, such as amorphous carbon, rGO, and N-rGO, are usually coated on Sn-based materials to buffer the volume change of these materials. In our study, we also used N-rGO as the substrate to support the Sn-based materials to avoid their capacity fading. However, as seen in Fig. 6d, the cycling behavior of the three Sn-based materials showed that only the SnS_2/N-rGO composite exhibited good stability. After 100 cycles, the reversible capacity of SnS_2/N-rGO was still 920.6 mA h g^{-1} with a capacity retention of 84.2%. On the contrary, the Sn/N-rGO and SnO_2/N-rGO composites deliver the poor cycling abilities with a reversible capacity retention of only 25.8% and 31.0% after 100 cycles. In general, the capacity fading was caused by the expansive volume excursions in the active electrode materials during the charging and discharging, leading to the pulverization of material and loss of electrical connectivity. Due to the mismatched structure of zero-dimensional Sn and SnO_2 nanoparticles with two-dimensional N-rGO, the electrode active materials are easily exfoliated during the charge/discharge process.[8] The SnS_2/N-rGO composite maintain good stability during the charge/discharge process due to its matched and robust structure formed between the two-dimensional layered SnS_2 and N-rGO.

Fig. 7a shows the rate cycling behavior of the three Sn-based composite electrodes. The high reversible capacity and excellent cycling behavior of the SnS_2/N-rGO composite are reflected in their high rate capabilities. The average specific capacities

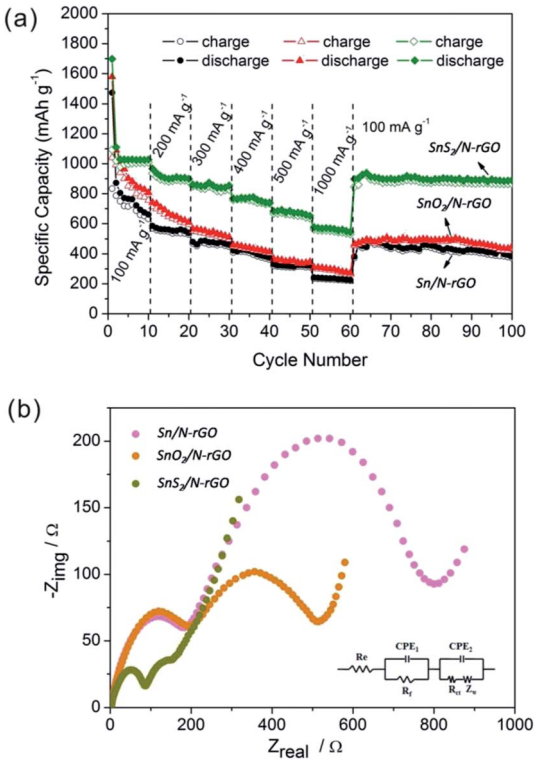

Fig. 7 (a) The cycling behavior of the Sn-based composites at various current densities and (b) their corresponding Nyquist plots. The inset shows the equivalent circuit model of the studied system and CPE represents the constant phase element, $Z_{CPE} = \{Q(j\omega)^n\}^{-1}$, $0 \le n \le 1$.

observed for the SnS_2/N-rGO composite are 1034, 918, 852, 772, 678, and 567 mA h g^{-1} at the current densities of 100, 200, 300, 400, 500, and 1000 mA g^{-1}, respectively. Remarkably, after cycling at 1000 mA g^{-1}, a stable capacity of ~900 mA h g^{-1} was still delivered when the current density was reduced back to 100 mA g^{-1}; this indicated high cycling stability. However, the Sn/N-rGO and SnO_2/N-rGO composites deliver a reversible capacity of only 200–300 mA h g^{-1} at a current density of 1000 mA g^{-1}, exhibiting a poor rate capability.

To further explain and better understand why the SnS_2/N-rGO electrode exhibits superior electrochemical performance as compared to the Sn/N-rGO and SnO_2/N-rGO electrodes, electrochemical impedance measurements have been performed after 3 cycles, as shown in Fig. 7b. The equivalent circuit model of the studied system is shown in the inset image of Fig. 7b.

The kinetic differences in the three Sn-based composite electrodes were further investigated by electrochemical impedance spectrum (EIS) modeling based on the modified equivalent circuit[46] using the fitted impedance parameters listed in Table 1.

In this model system, R_e represents the internal resistance of the test battery, R_f and CPE_1 are associated with the resistance and constant phase element of the SEI film, R_{ct} and CPE_2 are associated with the charge-transfer resistance and constant phase element of the electrode/electrolyte interface, respectively, and Z_W is associated with the Warburg impedance corresponding to the lithium-diffusion process. In Fig. 7b, the high

Table 1 The impedance parameters derived using an equivalent circuit model for Sn/N-rGO, SnO_2/N-rGO, and SnS_2/N-rGO

Electrodes	R_e (Ω)	R_f (Ω)	CPE_1 (μF)	R_{ct} (Ω)	CPE_2 (μF)
Sn/N-rGO	4.9	166.2	1.831	423.9	88.1
SnO_2/N-rGO	4.674	54.79	1.782	249.6	115.3
SnS_2/N-rGO	3.385	20.57	1.662	75.93	232

frequency semicircle corresponds to the resistance R_f and CPE_1 of the SEI film, and the semicircle in the medium frequency region is assigned to the charge-transfer resistance R_{ct} and CPE_2 of the electrode/electrolyte interface. The inclined line corresponds to the lithium-diffusion process within the bulk of the electrode material. From the analysis results, it is known that the SEI film resistance R_f and charge-transfer resistance R_{ct} of the SnS_2/N-rGO electrode material are 20.57 and 75.93 Ω, respectively, which are significantly lower than those found for the Sn/N-rGO and SnO_2/N-rGO electrodes. These results confirm that the structurally matched SnS_2/N-rGO composite can provide more active sites and greater electrolyte–electrode contact area for lithium ion insertion and extraction as compared to the others. The incorporation of N-rGO does not only preserve the high conductivity of the composite, but also greatly enhances the rapid electron transport during the electrochemical lithium insertion/extraction process. In particular, for the layer structured SnS_2/N-rGO composite, its robust structure ensures its stability during the high rate cycle, resulting in a significant improvement in the electrochemical performance of the SnS_2/N-rGO composite.

4. Conclusions

In summary, a series of tin-based materials (including Sn, SnO_2, and SnS_2) supported on N-rGO were successfully synthesized. When compared with pure rGO nanosheets, N-rGO provides more vacancies to provide nucleation sites for the Sn-based materials. The characterization results indicated that all the Sn-based materials were uniformly and tightly dispersed on the surface of N-rGO. In the three composites, the structural compatibility between the layer structured SnS_2 and N-rGO suggested the possibility of designing a robust electrode as an LIB anode without the deficiency of most rGO composites with 0D metal oxides. The LIB test results indicated that among three samples, the SnS_2/N-rGO composite delivered the highest specific reversible capacity (1093 mA h g^{-1}) with excellent cycling stability and high-rate capability. Upon comparing the three structural composites, it has been found that the impressive electrochemical performance observed for SnS_2/N-rGO can be attributed to its robust composite architecture that can withstand the stress of cycling as well as the complementary and synergistic interactions between the layered SnS_2 and N-rGO structures.

Conflicts of interest

There are no conflicts to declare.

Acknowledgements

This work was financially supported by the Natural Science Foundation of China (No. 51672071), the Natural Science Foundation of China for Young (No. 21303042), and Science and Technology Research Projects of Henan Provincial Department (No. 132102210256).

References

1 M. Winter and R. J. Brodd, *Chem. Rev.*, 2004, **104**, 4245–4269.
2 K. Chang, W. X. Chen, L. Ma, H. Li, H. Li, F. H. Huang, Z. D. Xu, Q. B. Zhang and J. Y. Lee, *J. Mater. Chem.*, 2011, **21**, 6251–6257.
3 K. Chang and W. X. Chen, *ACS Nano*, 2011, **5**, 4720–4728.
4 L. Shi, W. K. Wang, A. B. Wang, K. G. Yuan, Z. Q. Jin and Y. S. Yang, *J. Power Sources*, 2016, **318**, 184–191.
5 D. M. Kang, Q. L. Liu, R. Si, J. J. Gu, W. Zhang and D. Zhang, *Carbon*, 2016, **99**, 138–147.
6 Y. R. Ren and M. Q. Li, *J. Power Sources*, 2016, **306**, 459–466.
7 Y. Y. Li, H. Y. Zhang, Y. M. Chen, Z. C. Shi, X. G. Cao, Z. P. Guo and P. K. Shen, *ACS Appl. Mater. Interfaces*, 2016, **8**, 197–207.
8 K. Chang, Z. Wang, G. C. Huang, H. Li, W. X. Chen and J. Y. Lee, *J. Power Sources*, 2012, **201**, 259–266.
9 Y. H. Xu, J. C. Guo and C. S. Wang, *J. Mater. Chem.*, 2012, **22**, 9562–9567.
10 X. Xin, X. F. Zhou, F. Wang, X. Y. Yao, X. X. Xu, Y. M. Zhu and Z. P. Liu, *J. Mater. Chem.*, 2012, **22**, 7724–7730.
11 H. T. Kwon, C. K. Lee, K. J. Jeon and C. M. Park, *ACS Nano*, 2016, **10**, 5701–5709.
12 H. X. Yang and L. Li, *J. Alloys Compd.*, 2014, **584**, 76–80.
13 P. Zhao, W. B. Yue, Z. X. Xu, S. M. Sun and H. Y. Bao, *J. Alloys Compd.*, 2017, **704**, 51–57.
14 S. Z. Liang, X. F. Zhu, P. C. Lian, W. S. Yang and H. H. Wang, *J. Solid State Chem.*, 2011, **184**, 1400–1404.
15 K. Nishikawa, K. Dokko, K. Kinoshita, S. W. Woo and K. Kanamura, *J. Power Sources*, 2009, **189**, 726–729.
16 X. W. Lou, C. M. Li and L. A. Archer, *Adv. Mater.*, 2009, **21**, 2536–2539.
17 J. T. Zai, K. X. Wang, Y. Z. Su, X. F. Qian and J. S. Chen, *J. Power Sources*, 2011, **196**, 3650–3654.
18 Y. Z. Jiang, T. Z. Yuan, W. P. Sun and M. Yan, *ACS Appl. Mater. Interfaces*, 2012, **4**, 6216–6220.
19 J. Qin, C. N. He, N. Q. Zhao, Z. Y. Wang, C. S. Shi, E. Z. Liu and J. J. Li, *ACS Nano*, 2014, **8**, 1728–1738.
20 K. Zhang, H. Yang, M. Lü, C. Yan, H. Wu, A. Yuan and S. Lin, *J. Alloys Compd.*, 2018, **731**, 646–654.
21 K. Chang, D. S. Geng, X. F. Li, J. L. Yang, Y. J. Tang, M. Cai, R. Y. Li and X. L. Sun, *Adv. Energy Mater.*, 2013, **3**, 839–844.
22 G. X. Wang, B. Wang, X. L. Wang, J. Park, S. X. Dou, H. Ahn and K. Kim, *J. Mater. Chem.*, 2009, **19**, 8378–8384.
23 Y. M. Li, X. J. Lv, J. Lu and J. H. Li, *J. Phys. Chem. C*, 2010, **114**, 21770–21774.
24 L. S. Zhang, Y. P. Huang, Y. F. Zhang, W. Fan and T. X. Liu, *ACS Appl. Mater. Interfaces*, 2015, **7**, 27823–27830.

25 X. S. Zhou, J. C. Bao, Z. H. Dai and Y. G. Guo, *J. Phys. Chem. C*, 2013, **117**, 25367–25373.
26 X. Q. Xie, D. W. Su, J. Q. Zhang, S. Q. Chen, A. K. Mondal and G. X. Wang, *Nanoscale*, 2015, **7**, 3164–3172.
27 X. S. Zhou, L. J. Wan and Y. G. Guo, *Adv. Mater.*, 2013, **25**, 2152–2157.
28 F. H. Du, Y. S. Liu, J. Long, Q. C. Zhu, K. X. Wang, X. Wei and J. S. Chen, *Chem. Commun.*, 2014, **50**, 9961–9964.
29 J. Q. Shan, Y. X. Liu, P. Liu, Y. S. Huang, Y. Z. Su, D. Q. Wu and X. L. Feng, *J. Mater. Chem. A*, 2015, **3**, 24148–24154.
30 Q. Wang, L. Xing and X. Xue, *Mater. Lett.*, 2017, **209**, 155–158.
31 W. S. Hummers and R. E. Offeman, *J. Am. Chem. Soc.*, 1958, **80**, 1339.
32 D. S. Geng, Y. Chen, Y. G. Chen, Y. L. Li, R. Y. Li, X. L. Sun, S. Y. Ye and S. Knights, *Energy Environ. Sci.*, 2011, **4**, 760–764.
33 K. Chang, W. X. Chen, H. Li and H. Li, *Electrochim. Acta*, 2011, **56**, 2856–2861.
34 L. Wen, C. M. Liu, R. S. Song, H. Z. Luo, Y. Shi, F. Li and H. M. Cheng, *Acta Chim. Sin.*, 2014, **72**, 333–344.
35 Y. Jing, Z. Zhou, C. R. Cabrera and Z. F. Chen, *J. Mater. Chem. A*, 2014, **2**, 12104–12122.
36 C. Julien and C. PerezVicente, *Solid State Ionics*, 1996, **89**, 337–343.
37 C. Guan, X. H. Wang, Q. Zhang, Z. X. Fan, H. Zhang and H. J. Fan, *Nano Lett.*, 2014, **14**, 4852–4858.
38 J. Z. Chen, L. Yang, S. H. Fang, Z. X. Zhang, A. Deb and S. Hirano, *Electrochim. Acta*, 2014, **127**, 390–396.
39 M. Alaf and H. Akbulut, *J. Power Sources*, 2014, **247**, 692–702.
40 G. Kilibarda, S. Schlabach, V. Winkler, M. Bruns, T. Hanemann and D. V. Szabo, *J. Power Sources*, 2014, **263**, 145–153.
41 W. L. Yao, J. Yang, J. L. Wang and Y. Nuli, *J. Electrochem. Soc.*, 2008, **155**, A903–A908.
42 H. Nara, Y. Fukuhara, A. Takai, M. Komatsu, H. Mukaibo, Y. Yamauchi, T. Momma, K. Kuroda and T. Osaka, *Chem. Lett.*, 2008, **37**, 142–143.
43 H. Mukaibo, A. Yoshizawa, T. Momma and T. Osaka, *J. Power Sources*, 2003, **119**, 60–63.
44 H. B. Wang, T. Maiyalagan and X. Wang, *ACS Catal.*, 2012, **2**, 781–794.
45 D. Usachov, O. Vilkov, A. Gruneis, D. Haberer, A. Fedorov, V. K. Adamchuk, A. B. Preobrajenski, P. Dudin, A. Barinov, M. Oehzelt, C. Laubschat and D. V. Vyalikh, *Nano Lett.*, 2011, **11**, 5401–5407.
46 S. B. Yang, H. H. Song and X. H. Chen, *Electrochem. Commun.*, 2006, **8**, 137–142.

